

Cite this: *Mater. Adv.*, 2022,  
3, 6887

# Synergistic effect of nanosheet-array-like NiFe-LDH and reduced graphene oxide modified Ni foam for greatly enhanced oxygen evolution reaction and hydrogen evolution reaction†

Kun Wang, Jiawei Guo and Hui Zhang \*

Herein, we have prepared a series of highly efficient bifunctional electrocatalytic composites, Ni<sub>x</sub>Fe<sub>1-x</sub>-LDH/rGO/NF (x = 3, 2, 1), with vertically staggered NiFe-LDH nanosheets grown on nickel foam uniformly modified with reduced graphene oxide through a simple green hydrothermal method. The as-obtained nanosheet-array-like composites exhibit excellent performance for the oxygen evolution reaction (OER) and hydrogen evolution reaction (HER). In particular, Ni<sub>2</sub>Fe<sub>1</sub>-LDH/rGO/NF requires 228 and 109 mV for the OER and HER in 1 M KOH at 10 mA cm<sup>-2</sup>, respectively. Moreover, when it is directly used as both cathode and anode at the same time for overall water splitting, it only requires 1.62 V to achieve 10 mA cm<sup>-2</sup>. The as-prepared Ni<sub>2</sub>Fe<sub>1</sub>-LDH/rGO/NF composite shows excellent electrocatalytic performance, which is ascribed to the unique array-like nanosheet framework with exposed paths, the synergy between Ni<sub>2</sub>Fe<sub>1</sub>-LDH and rGO, and the vertically staggered growth of Ni<sub>2</sub>Fe<sub>1</sub>-LDH on the rGO/NF substrate improving the stability. This strategy can also be applied to create composites of other metal compositions with a nanosheet-array-like structure as efficient electrocatalysts for the development of efficient clean renewable energy.

Received 31st March 2022,  
Accepted 13th July 2022

DOI: 10.1039/d2ma00370h

rsc.li/materials-advances

## Introduction

With the current increase in demand for non-renewable fuels such as coal, oil and natural gas, the exploration and development of sustainable clean energy sources is one of the major issues facing researchers.<sup>1</sup> In order to eliminate the excessive dependence on traditional fossil energy and protect the environment in which we live, the development and use of clean and green renewable energy is very imperative.<sup>2</sup> Wind and solar energy are two main directions in the development of new energy sources, but their intermittency and time and space constraints have greatly affected their subsequent development. Therefore, it is necessary to develop a renewable energy source that is sustainable and not subject to seasonal and regional influences. Obviously, as a commercial technology, water splitting has great potential for obtaining environmentally friendly and sustainable energy.<sup>3</sup> There are two reactions involved in overall water splitting, namely, the oxygen evolution reaction (OER) and hydrogen evolution reaction (HER).<sup>4</sup> A complex

multi-proton coupled electron transfer process occurs in the OER reaction, resulting in slow kinetics and high overpotential, and this process is the rate-limiting step of overall water splitting.<sup>5</sup> The earliest considerable research efforts into OER catalysts with superior performance were dedicated to noble metal materials such as Ru, Ir, RuO<sub>2</sub> and IrO<sub>2</sub>,<sup>6</sup> and the best HER catalysts are Pt and its oxide, but these noble metal materials have huge disadvantages of high cost, scarcity and low dual-functionality for the OER and HER, limiting their large-scale commercial applications. In recent years, people have become committed to the design and synthesis of efficient, durable, low-cost and highly abundant transition metal substitutes, especially nickel,<sup>7-10</sup> iron,<sup>11,12</sup> cobalt<sup>13</sup> and the corresponding oxides,<sup>14</sup> hydroxides,<sup>15</sup> phosphides,<sup>16</sup> sulfides,<sup>17,18</sup> selenides<sup>19</sup> and nitrides.<sup>20</sup> As high-performance electrocatalysts, NiFe-based hydroxides/oxides have been extensively studied and are considered to be excellent electrocatalysts with low overpotential.

Layered double hydroxides (abbreviated as LDH) are layered inorganic materials that have the following structural characteristics: two-dimensional ordered layered structure, uniform dispersion of the main laminate elements, adjustable chemical composition of the main laminate, adjustable guest types and quantities and a diversity of structures, for which these compounds have attracted wide attention.<sup>21,22</sup> Various LDH materials with different compositions, such as NiFe LDH<sup>23,24</sup> and CoFe LDH,<sup>25</sup>

State Key Laboratory of Chemical Resource Engineering, Beijing University of Chemical Technology, Beijing, 100029, China. E-mail: zhanghui@buct.edu.cn, huizhang67@gst21.com

† Electronic supplementary information (ESI) available. See DOI: <https://doi.org/10.1039/d2ma00370h>

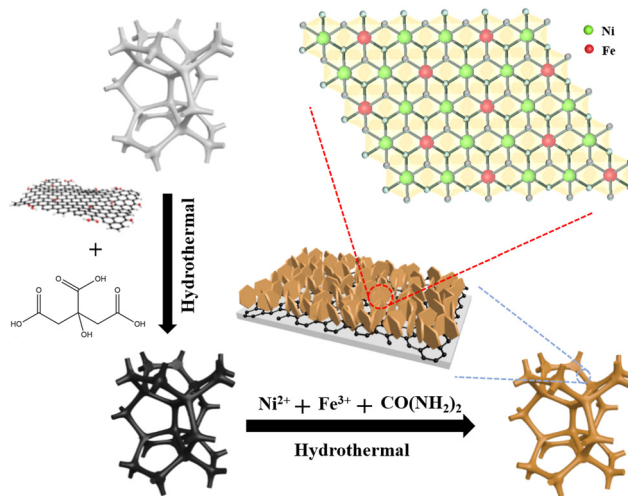


have been extensively studied in recent years. However, their active sites are less available due to their poor conductivity.<sup>26</sup> Carbon nanofibers,<sup>27</sup> carbon nanotubes<sup>28</sup> and graphene<sup>29</sup> have great potential in electrocatalysis owing to their large specific surface areas, satisfactory stability and conductivity. The combination of LDH and graphene is of important research significance, as it can significantly compensate for the low conductivity of LDH and further enhance its electrochemical catalytic activity. For instance, Xia *et al.* synthesized RGO-Ni-Fe LDH using a simple solvothermal method, which only requires 250 mV to achieve  $10 \text{ mA cm}^{-2}$ .<sup>30</sup> However, powder catalysts need to be fixed to conductive substrates with the help of adhesives, and this will reduce the contact area between the electrolyte and catalyst and the conductivity of the catalyst, which will inevitably reduce the electrocatalytic performance.<sup>31</sup> In addition, the catalyst will peel off the substrate because of its relatively weak binding force, especially under strong deflation conditions,<sup>32</sup> and the stability of the electrode will also be reduced. Nickel foam (NF) has been widely used as a base material.<sup>33</sup> Lu *et al.* reported a material using NF as the substrate to grow NiFe-LDH *in situ*, and the sample only required 280 mV at  $30 \text{ mA cm}^{-2}$  in the OER.<sup>34</sup> Li *et al.* prepared NiFe-LDH/RGO/NF through an ordinary electrodeposition strategy, and the overpotential for achieving  $10 \text{ mA cm}^{-2}$  during the OER process was only 150 mV. The excellent performance may have been due to the synergy of its large electrochemical active surface area and conductive RGO interface.<sup>35</sup> The catalyst synthesized by the electrodeposition method has a low yield and high requirements in terms of conditions, which is not suitable for large-scale commercial applications. Therefore, a need for improvement in preparation methods, catalytic performance, stability and applications remains. Thus, it is still a major issue in this field to obtain a bifunctional electrocatalyst that is suitable for commercial applications and shows outstanding overall water splitting performance using simpler methods and shorter time consumption.

In the present work, we develop an uncomplicated way to prepare array-like NiFe-LDH composites with vertically staggered nanosheets on rGO-modified NF using a hydrothermal method. The as-prepared composites, especially  $\text{Ni}_2\text{Fe}_1\text{-LDH/rGO/NF}$ , have a highly uniform nanosheet-array-like morphology decorated with tiny flowers, endowing the composite with strong synergy between  $\text{Ni}_2\text{Fe}_1\text{-LDH}$  and rGO/NF and structural stability. The vertically staggered growth of  $\text{Ni}_2\text{Fe}_1\text{-LDH}$  on the rGO/NF substrate is also favourable to the stability. The structure, composition, and macroscopic and microstructure morphology of all electrocatalysts were systematically characterized, and their electrochemical properties were also studied.  $\text{Ni}_2\text{Fe}_1\text{-LDH/rGO/NF}$  exhibits the highest electrochemical properties and excellent stability over at least 24 h, and its overall water splitting performance is greatly improved compared with those of recently reported electrocatalysts.

## Results and discussion

Scheme 1 illustrates the whole formation process schematically; the experimental details are presented in the ESI.†



Scheme 1 Schematic of the synthesis strategy of  $\text{Ni}_x\text{Fe}_1\text{-LDH/rGO/NF}$  ( $x = 3, 2, 1$ ) composites with nanosheet-array-like morphology.

The first step involving the modification of NF by rGO was reported in our previous work.<sup>36</sup> First, the proper amount of the prepared GO sol was placed in deionized water and ultrasonically treated to form an exfoliated GO suspension with good stability, and the proper amount of citric acid (CA) was added to the above GO suspension. Then, the obtained CA-GO suspension was reacted with NF under hydrothermal treatment, during which the etching of CA results in uniform coating of the reduced graphene oxide on the NF through electrostatic interactions. Simultaneously, CA plays a role in reducing GO during the treatment process. Subsequently, the LDH nanosheets were nucleated in an oriented fashion and were vertically staggered on the substrate *via* a hydrothermal process using nickel nitrate and iron nitrate as the metal sources and urea as the precipitant. The as-prepared  $\text{Ni}_x\text{Fe}_1\text{-LDH/rGO/NF}$  ( $x = 3, 2, 1$ ) composite electrocatalysts have a larger electrochemical specific surface area, as later results indicated, and higher electrical conductivity, which will greatly facilitate rapid electron transfer and electrolyte diffusion, thus enhancing their electrochemical performance.

The XRD patterns of the  $\text{Ni}_x\text{Fe}_1\text{-LDH/rGO/NF}$  ( $x = 3, 2, 1$ ) composites are shown in Fig. 1A. All the composites present strong and sharp diffraction peaks at  $2\theta$  values of  $44.5^\circ$ ,  $51.8^\circ$  and  $76.4^\circ$  indexed to the (111), (200) and (220) crystal planes of Ni foam (JCPDS 04-0850),<sup>37</sup> and small but detectable peaks corresponding to the (003) ( $11^\circ$ ) and (110) ( $59^\circ$ ) planes of the LDH phase ( $\text{Ni}_{0.75}\text{Fe}_{0.25}(\text{CO}_3)_{0.125}(\text{OH})_2 \cdot 0.38\text{H}_2\text{O}$  JCPDS 40-0215)<sup>38</sup> due to the masking of the extremely strong diffractions of NF. The patterns of scraped powder samples from the  $\text{Ni}_x\text{Fe}_1\text{-LDH/rGO/NF}$  ( $x = 3, 2, 1$ ) composites shown in Fig. 1B clearly display sharp and symmetrical characteristic diffractions at  $11.4^\circ$ ,  $22.9^\circ$ ,  $34.4^\circ$ ,  $45.9^\circ$ ,  $59.9^\circ$ ,  $61.3^\circ$  and  $65.1^\circ$  indexed to (003), (006), (012), (015), (018), (110) and (113) planes, respectively, and no other peaks of miscellaneous phases, implying that hexagonal NiFe-LDH was successfully synthesized in the obtained composites. The (003) peak with a basal spacing of 0.78 nm suggests the presence of



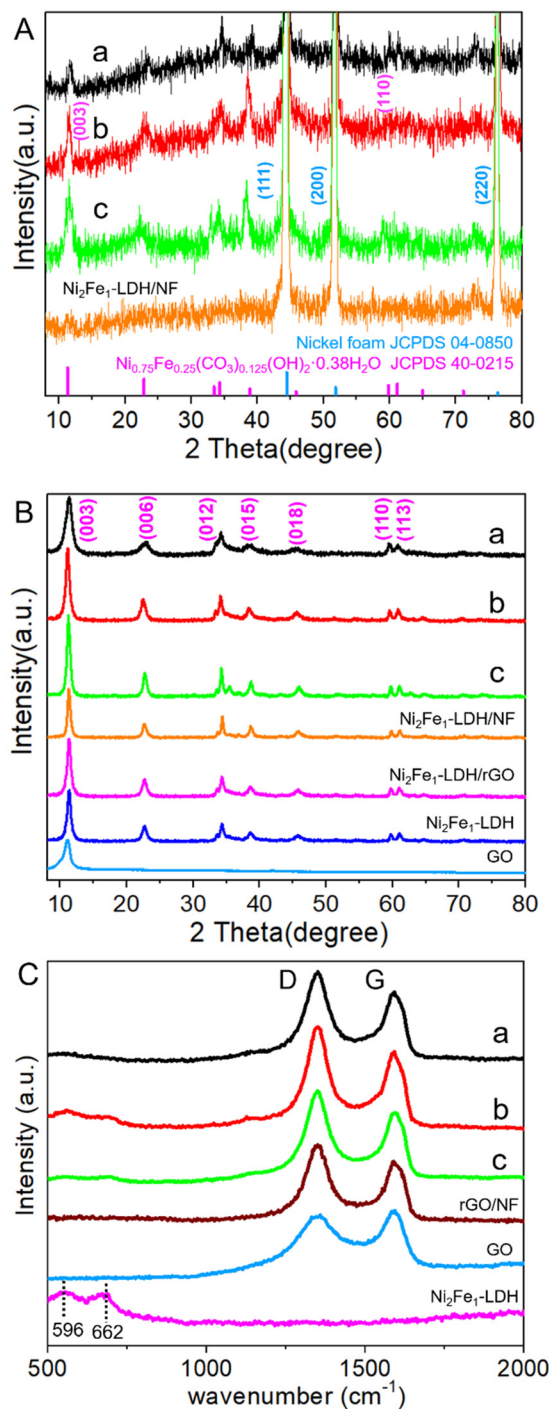


Fig. 1 XRD patterns (A and B) and Raman spectra (C) of the  $\text{Ni}_x\text{Fe}_1\text{-LDH/rGO/NF}$  ( $x = 3, 2, 1$ : a, b, c) composites (A and C) and the corresponding scraped powder samples (B) compared with those of  $\text{Ni}_2\text{Fe}_1\text{-LDH/NF}$ , rGO/NF, GO and  $\text{Ni}_2\text{Fe}_1\text{-LDH}$ .

interlayer  $\text{CO}_3^{2-}$  anions, and the sharp (110) and (113) lines imply the ordered atomic dispersion state of metal cations on the LDH layers. It is also noted that the obvious peak at  $\sim 11^\circ$  (0.85 nm) corresponding to the (001) plane of GO<sup>36,39,40</sup> disappears in the composites, implying the transformation of GO into rGO; this phenomenon is attributed to the reduction in the

alkaline synthetic environment, and the change is beneficial for the improvement of the conductivity of the material. These findings clearly demonstrate the homogeneous combination of a well-crystallized LDH phase and rGO/NF. Table S1 (ESI<sup>†</sup>) shows the XRD structure parameters of the powder samples of the composites. The  $D_{110}$  data of the  $\text{Ni}_x\text{Fe}_1\text{-LDH/rGO/NF}$  ( $x = 3, 2, 1$ ) composites calculated according to the Scherrer formula are 21.63, 24.75 and 29.74 nm, respectively. From this, along with the strength and symmetry of the diffractions, it can be inferred that  $\text{Ni}_2\text{Fe}_1\text{-LDH/rGO/NF}$  possesses higher crystallinity and relatively smaller crystalline size.

The Raman spectra presented in Fig. 1C strongly verify the existence of rGO in the composites. The two obvious Raman bands at  $1350$  and  $1592\text{ cm}^{-1}$  represent the D-band associated with the defect sites at the edge of graphene and the G-band related to the in-plane vibration of  $\text{sp}^2$  carbon atoms for carbon materials, respectively. The strength ratio of the D-band to the G-band ( $I_D/I_G$ ) is generally applied to measure the degree of disorder of carbon and the average size of the  $\text{sp}^2$  region,<sup>41</sup> and thus, the graphitization degree of the composites. The higher  $I_D/I_G$  value of  $\text{Ni}_2\text{Fe}_1\text{-LDH/rGO/NF}$  (1.26) compared with that of GO indicates that the graphitization degree of the composites is higher than that of the original GO (0.95), which was attributed to the unrepaired defect sites generated during the reduction of GO to rGO. The highest  $I_D/I_G$  value of  $\text{Ni}_2\text{Fe}_1\text{-LDH/rGO/NF}$  indicates that it has the most abundant defect sites, which can provide more catalytically active sites. In addition, the two weak bands near  $596$  and  $662\text{ cm}^{-1}$  are attributed to Ni-O and Fe-O symmetric stretching vibrations, respectively.

The constructions of the composites were analyzed using SEM to further observe the morphologies. The SEM and (HR)TEM images of the  $\text{Ni}_x\text{Fe}_1\text{-LDH/rGO/NF}$  ( $x = 3, 2, 1$ ) composites, along with the EDS and elemental mappings, are shown in Fig. 2, and the SEM images of NF, the substrate rGO/NF and  $\text{Ni}_2\text{Fe}_1\text{-LDH/NF}$  are shown in Fig. S1 and S2 (ESI<sup>†</sup>). The bare Ni foam showed a smoother surface, which consisted of some interconnected pores, which is favourable for providing abundant electron channels and large contact area between the electrolyte and the electrode material. The rGO/NF results show that after modification with rGO, the small holes disappeared

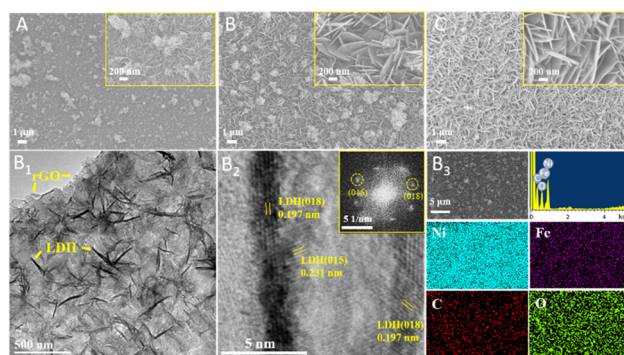


Fig. 2 SEM images of  $\text{Ni}_x\text{Fe}_1\text{-LDH/rGO/NF}$  ( $x = 3, 2, 1$ : A, B, C), and TEM ( $B_1$ ), HRTEM ( $B_2$ , inset: FFT), EDS and elemental mapping ( $B_3$ ) of  $\text{Ni}_2\text{Fe}_1\text{-LDH/rGO/NF}$ .



and an rGO tier was present on the surface of the NF, with obvious rGO sheet layer wrinkles on the surface. The composites  $\text{Ni}_x\text{Fe}_1\text{-LDH/rGO/NF}$  ( $x = 3, 2, 1$ ) (Fig. 2(A–C)) clearly present an array-like morphology with a large number of vertically staggered LDH nanosheets grown on the substrate.

In detail, the  $\text{Ni}_3\text{Fe}_1\text{-LDH/rGO/NF}$  composite with small LDH nanosheets of  $\sim 195 \times 25.6$  nm shows poor uniformity with obviously agglomerated particles. With the decrease of the Ni/Fe molar ratio, the size and thickness of the LDH nanosheets gradually increased, in line with the XRD data. The  $\text{Ni}_1\text{Fe}_1\text{-LDH/rGO/NF}$  composite shows enlarged and thickened LDH nanosheets ( $\sim 742 \times 76.7$  nm) that are intimately stacked together. The  $\text{Ni}_2\text{Fe}_1\text{-LDH/rGO/NF}$  composite exhibits a clear vertically staggered nanosheet array morphology decorated with a small amount of tiny, loosely aggregated flowers on hexagonal LDH nanosheets with moderate size and thickness ( $\sim 626 \times 37.5$  nm) and abundant open spaces. Compared with the non-rGO modified composite  $\text{Ni}_2\text{Fe}_1\text{-LDH/NF}$  ( $\sim 1.6 \times 0.1$   $\mu\text{m}$ ), the size of the LDH nanosheets in  $\text{Ni}_2\text{Fe}_1\text{-LDH/rGO/NF}$  is also obviously smaller (Fig. S2, ESI<sup>†</sup>).

The TEM image of  $\text{Ni}_2\text{Fe}_1\text{-LDH/rGO/NF}$  (Fig. 2B<sub>1</sub>) further reveals the nanosheet array morphology decorated with small flowers on the surface of the rGO. The HRTEM result in Fig. 2B<sub>2</sub> shows lattice fringes of 0.231 and 0.197 nm, which were indexed to the (015) and (018) planes of  $\text{Ni}_2\text{Fe}_1\text{-LDH}$  nanosheets. Due to the influence of the Ni foam, the Ni:Fe atomic ratio of  $\text{Ni}_2\text{Fe}_1\text{-LDH/rGO/NF}$  obtained using EDS was 3.56 : 1. We used ICP to obtain a more accurate element ratio, and the obtained proportion was 1.95 : 1, which is close to that of the feedstocks. The elemental mappings (Fig. 2B<sub>3</sub>) indicate the uniform distribution of the elements Ni, Fe, C and O on the  $\text{Ni}_2\text{Fe}_1\text{-LDH/rGO/NF}$  composite. The relatively sparse dots in the image of the element C are consistent with the vertically staggered coverage of LDH nanosheets.

Based on the above microstructural features of the composites, it can be envisioned that their mechanical stability and durability may be greatly enhanced by the present network with abundant open space and high openness. Thus, the as-prepared novel composite electrodes can increase the effective contact area with the electrolyte, thereby promoting the rapid dispersion of electrochemical active substances and effective electron transfer, which is favorable for water splitting.

XPS characterization was used to study the electrocatalyst to further explore the possible chemical valence states and surface composition of the composites. The full XPS spectra of the  $\text{Ni}_x\text{Fe}_1\text{-LDH/rGO/NF}$  ( $x = 3, 2, 1$ ) composites (Fig. S3, ESI<sup>†</sup>) clearly affirm the presence of nickel, iron, carbon and oxygen. The XPS narrow spectra of the samples are presented in Fig. 3. Ni 2p XPS shows peaks at  $\sim 874.7$  and  $\sim 857.0$  eV, which were attributed to Ni 2p<sub>1/2</sub> and Ni 2p<sub>3/2</sub>,<sup>42</sup> respectively, and the corresponding satellite peaks at  $\sim 880.9$  and  $862.8$  eV, implying the existence of Ni<sup>2+</sup> in all the samples. It is noted that the BE of Ni 2p<sub>3/2</sub> of  $\text{Ni}_2\text{Fe}_1\text{-LDH/NF}$  is 856.10 eV,  $\sim 0.3$  eV lower than that of pure  $\text{Ni}_2\text{Fe}_1\text{-LDH}$  (856.40 eV), showing an increase in the electron density of the Ni<sup>2+</sup> core level after the introduction of NF. The BE values of Ni 2p<sub>3/2</sub> of the three composites

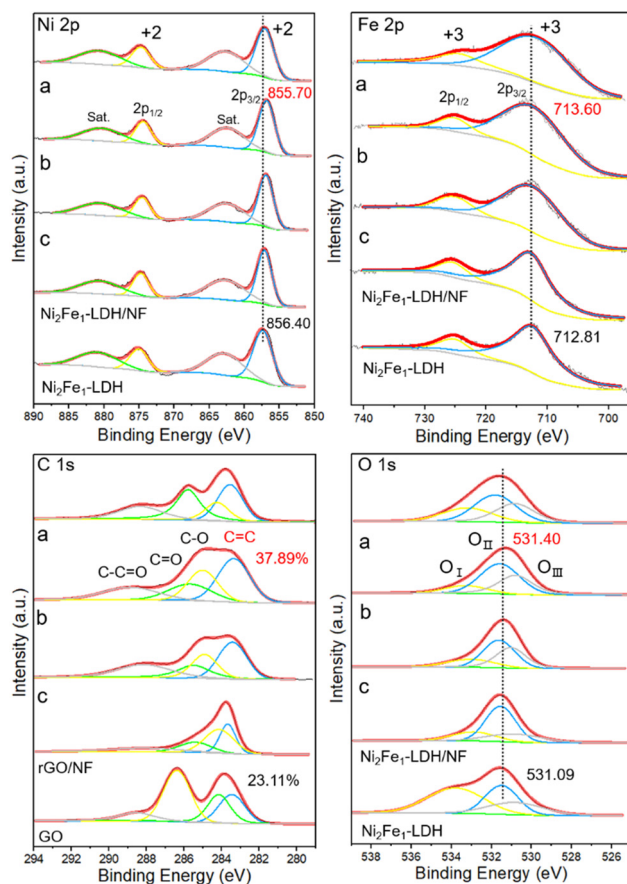


Fig. 3 Ni 2p, Fe 2p, C 1s and O 1s XPS spectra of  $\text{Ni}_x\text{Fe}_1\text{-LDH/rGO/NF}$  ( $x = 3, 2, 1$ : a, b, c) composites and  $\text{Ni}_2\text{Fe}_1\text{-LDH/NF}$ ,  $\text{Ni}_2\text{Fe}_1\text{-LDH}$ , rGO/NF and GO.

$\text{Ni}_x\text{Fe}_1\text{-LDH/rGO/NF}$  ( $x = 3, 2, 1$ ) are 856.00, 855.70 and 855.91 eV, respectively, which are 0.4, 0.7 and 0.49 eV lower than that of  $\text{Ni}_2\text{Fe}_1\text{-LDH}$ , respectively, demonstrating the obviously improved proportion of Ni<sup>2+</sup>, and  $\text{Ni}_2\text{Fe}_1\text{-LDH/rGO/NF}$  has the greatest upshift. The protruding peaks at  $\sim 726.4$  and  $\sim 713.6$  eV seen in the Fe 2p XPS are attributed to Fe 2p<sub>1/2</sub> and Fe 2p<sub>3/2</sub>,<sup>43</sup> respectively, affirming the existence of Fe<sup>3+</sup>. The BE value of Fe 2p<sub>3/2</sub> of  $\text{Ni}_2\text{Fe}_1\text{-LDH/NF}$  is 713.00 eV, which is 0.19 eV higher than that for  $\text{Ni}_2\text{Fe}_1\text{-LDH}$  (712.81 eV), demonstrating that the combination of LDH and NF clearly reduces the electron density of Fe<sup>3+</sup>. In addition, the BE values of Fe 2p<sub>3/2</sub> of the three composites  $\text{Ni}_x\text{Fe}_1\text{-LDH/rGO/NF}$  ( $x = 3, 2, 1$ ) are 713.30, 713.60, and 713.40 eV, respectively, which are 0.49, 0.79, and 0.59 eV higher than that of  $\text{Ni}_2\text{Fe}_1\text{-LDH}$ , respectively, indicating a decrease in the electron density of Fe<sup>3+</sup>, with  $\text{Ni}_2\text{Fe}_1\text{-LDH/rGO/NF}$  having the largest decrease. Based on these results, an obvious Ni–Fe synergistic effect exists in the composites due to electron transfer from Fe cores to Ni cores. The strongest synergy of  $\text{Ni}_2\text{Fe}_1\text{-LDH/rGO/NF}$  indicates the best activity.

The C 1s XPS spectra of all the samples can be deconvoluted into four peaks assigned to C=C, C=O, C–O and O–C=O at BE values (eV) of 284.6, 286.4, 285.4 and 288.9, respectively.<sup>44</sup>

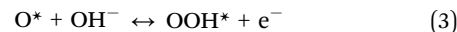
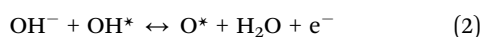
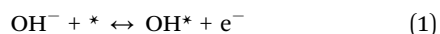


The proportion of C=C functional groups of rGO/NF (27.32%) is significantly higher than that of the initial GO (23.11%), indicating the partial reduction of the GO. The C=C contents of Ni<sub>3</sub>Fe<sub>1</sub>-LDH/rGO/NF (30.97%), Ni<sub>2</sub>Fe<sub>1</sub>-LDH/rGO/NF (37.89%) and Ni<sub>1</sub>Fe<sub>1</sub>-LDH/rGO/NF (33.73%) are all higher than the initial GO (23.11%), consistent with the above Raman results, suggesting that more GO was converted to rGO in the synthesis environment, thus improving the conductivity. The C=C content of Ni<sub>2</sub>Fe<sub>1</sub>-LDH/rGO/NF had the largest increase, indicating the strongest interaction between Ni<sub>2</sub>Fe<sub>1</sub>-LDH and the substrate.

The O 1s XPS spectra of all the samples can be deconvoluted into three peaks (Fig. 3) ascribed to the hydroxyl group (O<sub>I</sub>) in H<sub>2</sub>O (~532.8 eV), the M-OH group (~531.8 eV) (O<sub>II</sub>) and the M-O (M = Ni, Fe) group (O<sub>III</sub>) on the LDH layer (~531.0 eV).<sup>45</sup> The BE value of the M-OH group of Ni<sub>2</sub>Fe<sub>1</sub>-LDH/NF is 531.11 eV, which is 0.02 eV higher than that of 531.09 eV of Ni<sub>2</sub>Fe<sub>1</sub>-LDH, indicating the reduced electron density of the M-OH group of LDH grown on NF. For the Ni<sub>x</sub>Fe<sub>1</sub>-LDH/rGO/NF (x = 3, 2, 1) composites, the BE values of the M-OH group are 531.19, 531.40 and 531.20 eV, which are 0.1, 0.31 and 0.11 eV higher than that of Ni<sub>2</sub>Fe<sub>1</sub>-LDH (531.09 eV), respectively, in which Ni<sub>2</sub>Fe<sub>1</sub>-LDH/rGO/NF exhibits the biggest upshift, implying that its M-OH groups have the lowest electron density. In addition, the M-O contents of Ni<sub>3</sub>Fe<sub>1</sub>-LDH/rGO/NF (30.86%), Ni<sub>2</sub>Fe<sub>1</sub>-LDH/rGO/NF (35.83%), Ni<sub>1</sub>Fe<sub>1</sub>-LDH/rGO/NF (33.73%) and Ni<sub>2</sub>Fe<sub>1</sub>-LDH/NF (23.07%) are all higher than that of Ni<sub>2</sub>Fe<sub>1</sub>-LDH (22.47%).

All the above results tentatively reveal the existence of interaction between the electrons of the composites, and further demonstrate the synergistic impact of Ni-Fe, which has a positive effect on adjusting the electronic environment of the Ni and Fe species, and indicate there is likely to be an improvement in the electrocatalytic activity. In addition, the electrical conductivity could be improved due to the change from GO to rGO, thereby increasing the electrical conductivity and further improving the electrocatalytic performance of the composites.

The OER performances of all the composites and control samples were tested in 1 M KOH. All the polarization curves acquired were corrected with 90% iR compensation.<sup>46</sup> The results showed that Ni<sub>2</sub>Fe<sub>1</sub>-LDH/rGO/NF possesses the most prominent OER behavior, requiring only 228 mV at 10 mA cm<sup>-2</sup>, and its performance is clearly better than those of Ni<sub>3</sub>Fe<sub>1</sub>-LDH/rGO/NF (256 mV), Ni<sub>1</sub>Fe<sub>1</sub>-LDH/rGO/NF (244 mV), Ni<sub>2</sub>Fe<sub>1</sub>-LDH/NF (283 mV), Ni<sub>2</sub>Fe<sub>1</sub>-LDH/rGO (323 mV), Ni<sub>2</sub>Fe<sub>1</sub>-LDH (371 mV), the substrate rGO/NF (390 mV), pure NF (455 mV) and RuO<sub>2</sub> (350 mV) (Fig. 4A, C, D and F). As shown in Fig. 4B and E, the Tafel slope (mV dec<sup>-1</sup>) of Ni<sub>2</sub>Fe<sub>1</sub>-LDH/rGO/NF is only 37.9, which is clearly smaller than those of Ni<sub>3</sub>Fe<sub>1</sub>-LDH/rGO/NF (55.3), Ni<sub>1</sub>Fe<sub>1</sub>-LDH/rGO/NF (47.3), Ni<sub>2</sub>Fe<sub>1</sub>-LDH/NF (77.2), rGO/NF (139.7), NF (179.1) and RuO<sub>2</sub> (180), giving further confirmation of its superior OER performance. The specific steps for excellent electrochemical performance can be summarized as follows:<sup>47</sup>



where \* represents the active site, and OH\*, O\* and OOH\* are adsorbed intermediate species. Step one shown in eqn (1) is the adsorption of the first OH<sup>-</sup>, followed by the reaction with the second one (eqn (2)). The combination of O\* and OH<sup>-</sup> then occurs for the synthesis of OOH\* (eqn (3)), eventually producing oxygen (eqn (4)). There is a synergy between Ni and Fe atoms, which can effectively adjust the electronic structure and the relative adsorption intensity of the three intermediates, and the activities of the composites can be further increased. The excellent OER performance of Ni<sub>2</sub>Fe<sub>1</sub>-LDH/rGO/NF is comparable to those of most non-precious transition metal materials (Fig. 4I and Table S3, ESI<sup>†</sup>). The fitted data of the impedimetric parameters of the EIS measurement are listed in Table S2 (ESI<sup>†</sup>). Clearly, the charge transfer resistance (*R*<sub>ct</sub>, Ω cm<sup>-2</sup>) of Ni<sub>2</sub>Fe<sub>1</sub>-LDH/rGO/NF (7.51) is lower than those of Ni<sub>3</sub>Fe<sub>1</sub>-LDH/rGO/NF (16.3), Ni<sub>1</sub>Fe<sub>1</sub>-LDH/rGO/NF (11.5) and Ni<sub>2</sub>Fe<sub>1</sub>-LDH/NF (18.5), implying that it has the fastest charge transfer capability, in accordance with the smaller diameter of the impedance arc (Fig. 4G). Together with the OER performance and lowest Tafel slope, these findings affirm that the synergy between Ni<sub>2</sub>Fe<sub>1</sub>-LDH and the substrate is beneficial to the kinetics.

As shown in Fig. 4H, there is almost no decay in the overpotential of Ni<sub>2</sub>Fe<sub>1</sub>-LDH/rGO/NF for the OER after the tests, indicating its comparative superior stability and robustness. The inset curves in Fig. 4H show that the LSV curve is close to the original curve, and that there is only a slight rise in the overpotential after the test. This slight change may be attributed to the slightly reduced specific surface area, subtle aggregation and mutual adhesion of the nanosheets, which are not conducive to mass transfer, resulting in the reduction in the performance. The detectably reduced size and thickness of the LDH nanosheets (Fig. S4, ESI<sup>†</sup>) is likely to be related to the gas continuously released from the electrocatalyst and partial etching in strong alkaline solution, leading to the shedding of the catalyst, and thus a reduction in the weight of the active material.

The HER performances of all the electrocatalysts were further examined. Moreover, the electrocatalytic properties of the commercially available benchmark 20% Pt/C were measured under identical testing conditions. Surprisingly, as displayed in Fig. 5A, C, D and F, the overpotential of Ni<sub>2</sub>Fe<sub>1</sub>-LDH/rGO/NF is only 109 mV at 10 mA cm<sup>-2</sup>, which is inferior to that of 20% Pt/C (20 mV), but extremely improved compared to those of Ni<sub>3</sub>Fe<sub>1</sub>-LDH/rGO/NF (131 mV), Ni<sub>1</sub>Fe<sub>1</sub>-LDH/rGO/NF (117 mV), Ni<sub>2</sub>Fe<sub>1</sub>-LDH/NF (151 mV), Ni<sub>2</sub>Fe<sub>1</sub>-LDH/rGO (159 mV), Ni<sub>2</sub>Fe<sub>1</sub>-LDH (162 mV), the substrate rGO/NF (170 mV) and pure NF (192 mV), implying the outstanding HER activity of Ni<sub>2</sub>Fe<sub>1</sub>-LDH/rGO/NF in alkaline solution. The Tafel slope (mV dec<sup>-1</sup>) of Ni<sub>2</sub>Fe<sub>1</sub>-LDH/rGO/NF (121.1) is lower than those of Ni<sub>3</sub>Fe<sub>1</sub>-LDH/rGO/NF (143.4), Ni<sub>1</sub>Fe<sub>1</sub>-LDH/rGO/NF (130.6), Ni<sub>2</sub>Fe<sub>1</sub>-LDH/NF (152.2), the substrate rGO/NF (171.1) and pure NF (182.8) (Fig. 5B and E), implying its excellent HER activity. The mechanism for HER can be summarized as the Volmer



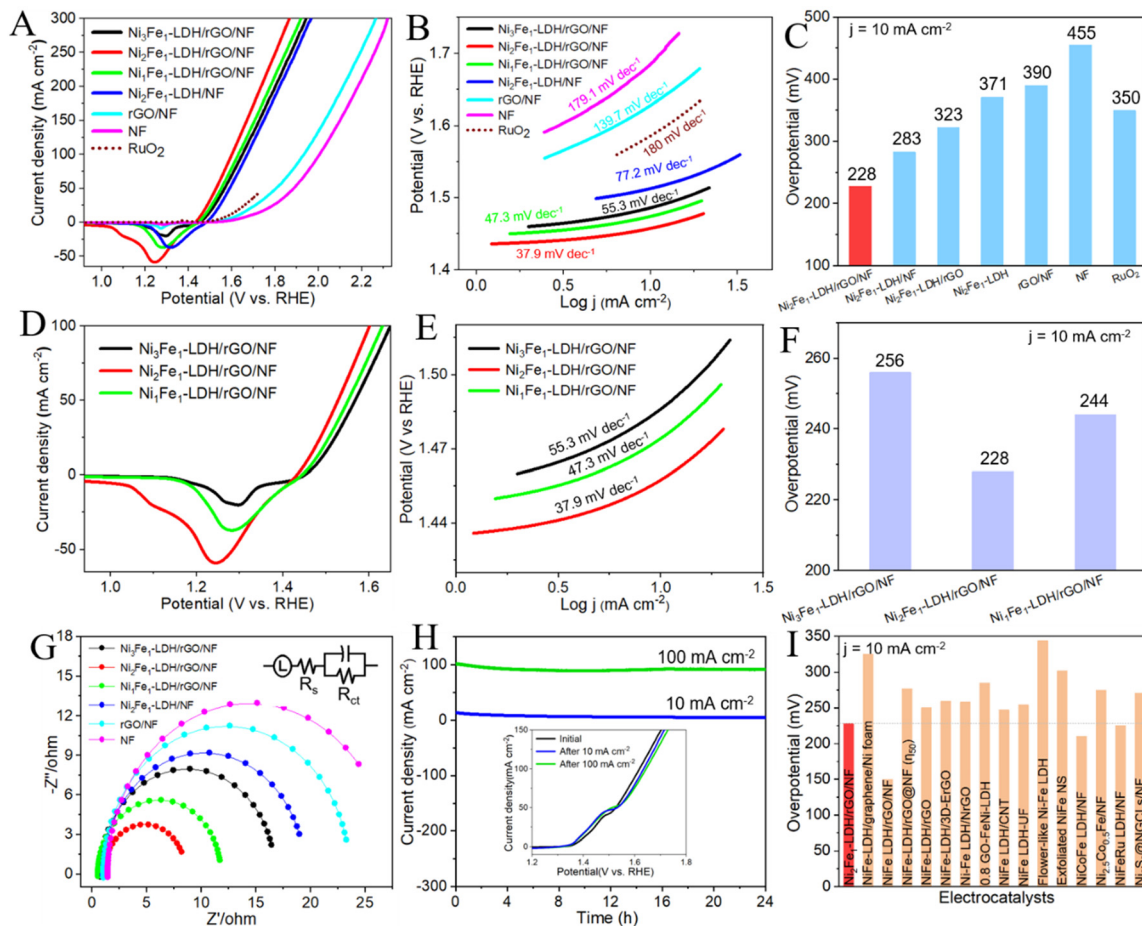
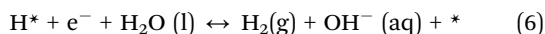


Fig. 4 (A) OER polarization curves, (B) Tafel plots, and (C) performance comparison chart for the OER of the  $\text{Ni}_x\text{Fe}_1\text{-LDH/rGO/NF}$  ( $x = 3, 2, 1$ ) composites and control samples. (D–F) are the corresponding detailed charts of the  $\text{Ni}_x\text{Fe}_1\text{-LDH/rGO/NF}$  ( $x = 3, 2, 1$ ) composites. (G) Nyquist plots. (H) Chronoamperometry measurements of the  $\text{Ni}_2\text{Fe}_1\text{-LDH/rGO/NF}$  composite over 24 h at 10 and 100  $\text{mA cm}^{-2}$  (inset: OER comparison before and after the test). (I) OER performance comparison in 1 M KOH.

(eqn (5))–Heyrovsky (eqn (6)) mechanism given below in alkaline solution:<sup>48</sup>



where \* represents the active site, and  $\text{H}^*$  is the species of adsorbed H. As shown in eqn (5), the discharge process of  $\text{H}_2\text{O}$  from the electrocatalyst surface produces the hydrogen intermediates ( $\text{H}^*$ ) in an alkaline electrolyte, and the production of hydrogen occurs *via* a process known as electrochemical desorption (eqn (6)). The obtained outcomes affirm that the synergy of Ni–Fe can effectively optimize the electronic structure of the electrocatalyst and thus enhance its HER activity. As shown in Fig. 5I and Table S5 (ESI<sup>†</sup>), the  $\text{Ni}_2\text{Fe}_1\text{-LDH/rGO/NF}$  composite is competitive compared with most transition metal electrocatalysts for the HER. The  $R_{\text{ct}}$  ( $\Omega \text{ cm}^{-2}$ ) value of  $\text{Ni}_2\text{Fe}_1\text{-LDH/rGO/NF}$  (7.63) is lower than those of  $\text{Ni}_3\text{Fe}_1\text{-LDH/rGO/NF}$  (26.8),  $\text{Ni}_1\text{Fe}_1\text{-LDH/rGO/NF}$  (16.1) and  $\text{Ni}_2\text{Fe}_1\text{-LDH/NF}$  (37.7) (Table S4, ESI<sup>†</sup>), as can also be concluded from its smaller semicircle in the Nyquist plot (Fig. 5G). The advantages of

$\text{Ni}_2\text{Fe}_1\text{-LDH/rGO/NF}$  are in accordance with its best HER activity and lowest Tafel slope.

Fig. 5H reveals that the overpotential exhibits almost no decay after the stability measurement of  $\text{Ni}_2\text{Fe}_1\text{-LDH/rGO/NF}$  for the HER, maintaining stable electrocatalytic activity in alkaline solution. Subsequently, we compared the LSV curves and SEM images of  $\text{Ni}_2\text{Fe}_1\text{-LDH/rGO/NF}$  before and after the stability measurements. It can be seen from the inset curves that the LSV curve after the test is similar to the original one and that there is no obvious decline in current density. It can be seen from the SEM images that although there is slight agglomeration, the nanosheet array morphology is still relatively complete (Fig. S5, ESI<sup>†</sup>), so the electrocatalytic performance is not significantly reduced. The LDH loading amount was obtained using thermogravimetric analysis (TGA, Fig. S9, ESI<sup>†</sup>), and the calculated data for the loading of LDH on the rGO/NF of  $\text{Ni}_x\text{Fe}_1\text{-LDH/rGO/NF}$  ( $x = 3, 2, 1$ ) composites and control sample  $\text{Ni}_2\text{Fe}_1\text{-LDH/NF}$  are 6.21, 5.19, 5.86 and 4.14  $\text{mg cm}^{-2}$ , respectively. The above findings can help us to understand the excellent HER performance of  $\text{Ni}_2\text{Fe}_1\text{-LDH/rGO/NF}$  with good long-term stability.



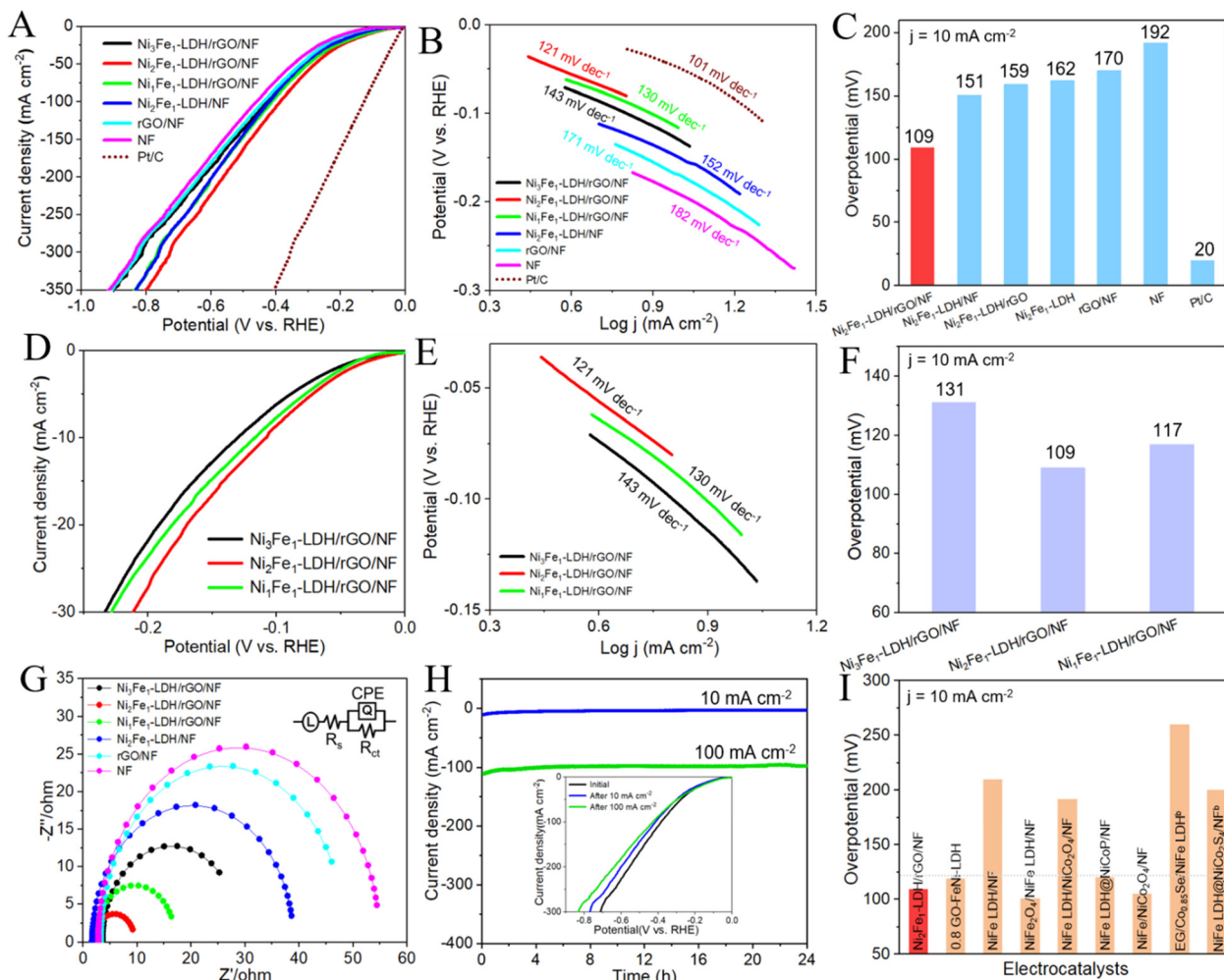


Fig. 5 (A) HER polarization curves, (B) Tafel plots, and (C) performance comparison chart for the HER of the  $Ni_xFe_1$ -LDH/rGO/NF ( $x = 3, 2, 1$ ) composites and control samples. (D–F) are the corresponding detailed charts of the  $Ni_xFe_1$ -LDH/rGO/NF ( $x = 3, 2, 1$ ) composites. (G) Nyquist plots. (H) Chronoamperometry measurements of the  $Ni_2Fe_1$ -LDH/rGO/NF composite over 24 h at 10 and 100  $mA\ cm^{-2}$  (inset: HER comparison before and after the test). (I) HER performance comparison in 1 M KOH.

We further analyzed the samples of  $Ni_2Fe_1$ -LDH/rGO/NF after the stability measurements using XPS to study the changes in the chemical valence states (Fig. S8, ESI<sup>†</sup>). For the OER, the two prominent peaks near 854.8 and 873.6 eV were attributed to the  $2p_{3/2}$  and  $2p_{1/2}$  of  $Ni^{2+}$ , and the prominent peaks near 856.8 and 877.2 eV were attributed to the  $2p_{3/2}$  and  $2p_{1/2}$  of  $Ni^{3+}$ , indicating that the  $Ni^{2+}$  on the surface was partially oxidized to  $Ni^{3+}$  during the OER. The  $Ni^{2+}/Ni^{3+}$  ratio is 5.42 and 0.35 at 10 and 100  $mA\ cm^{-2}$ , respectively, indicating that  $Ni^{2+}$  will be more oxidized to  $Ni^{3+}$  due to the violent release of oxygen bubbles at high current densities. In the Fe 2p XPS, no significant changes occurred. In the C 1s XPS, the ratios of oxygen-containing groups were 64.93% and 86.55% at 10 and 100  $mA\ cm^{-2}$ , respectively, increasing by 2.82% and 24.44% compared to before, indicating that the higher the current density, the greater the amount of carbon corroded and the greater the proportion of oxygen-containing groups. Although the change had no obvious effect on the performance of the composite, because more oxygen-containing groups can decrease

the stability of the structure, there will probably be a certain impact on the durability of the catalysts. After the OER stability test at 10  $mA\ cm^{-2}$ , the ratios of  $O_{II}$  and  $O_{III}$  changed by  $-4.72\%$  and  $1.15\%$ , respectively, and the ratios of  $O_{II}$  and  $O_{III}$  changed by  $-1.31\%$  and  $-5.06\%$  at 100  $mA\ cm^{-2}$ , respectively, implying that M-OOH (M = Ni, Fe) was formed on the surface of the composite (Table S6, ESI<sup>†</sup>). For the HER, none of the valence states of the four elements changed significantly, indicating the excellent stability of  $Ni_2Fe_1$ -LDH/rGO/NF for the HER.<sup>49</sup>

The electrochemical surface area (ECSA) is determined using cyclic voltammetry. The double-layer capacitance ( $C_{dl}$ ,  $mF\ cm^{-2}$ ) of  $Ni_2Fe_1$ -LDH/rGO/NF was 81.5, which is better than those of  $Ni_3Fe_1$ -LDH/rGO/NF (47.4) and  $Ni_1Fe_1$ -LDH/rGO/NF (71.6) (Fig. S6, ESI<sup>†</sup>), and is nearly two, four and six times higher than those of  $Ni_2Fe_1$ -LDH/NF (41.5), the substrate rGO/NF (17.8) and pure NF (13.2) (Fig. S7, ESI<sup>†</sup>), respectively. It is well known that a high  $C_{dl}$  value represents an increase in ECSA, indicating the highest intrinsic activity of  $Ni_2Fe_1$ -LDH/rGO/NF. We further calculated the ECSA to confirm the



excellent performance of the electrocatalyst. The ECSA values of the composites were obtained using the following equation:  $ECSA = C_{dl}/C_s$ , where  $C_s$  ( $0.040 \text{ mF cm}^{-2}$ ) is the specific capacitance in alkaline electrolyte, and the ECSA is directly proportional to  $C_{dl}$ . The ECSA of  $\text{Ni}_2\text{Fe}_1\text{-LDH/rGO/NF}$  obtained using the equation is 2037.5, which is greater than those of  $\text{Ni}_3\text{Fe}_1\text{-LDH/rGO/NF}$  (1185) and  $\text{Ni}_1\text{Fe}_1\text{-LDH/rGO/NF}$  (1790), suggesting better electrocatalytic performance. In addition, the TOF values of  $\text{Ni}_2\text{Fe}_1\text{-LDH/rGO/NF}$  are 0.153 and  $0.077 \text{ s}^{-1}$  for the OER and HER at an overpotential of 300 mV, respectively, which are obviously higher than those of  $\text{Ni}_3\text{Fe}_1\text{-LDH/rGO/NF}$  (0.102 and  $0.033 \text{ s}^{-1}$ , respectively),  $\text{Ni}_1\text{Fe}_1\text{-LDH/rGO/NF}$  (0.128 and  $0.056 \text{ s}^{-1}$ , respectively) and  $\text{Ni}_2\text{Fe}_1\text{-LDH/NF}$  (0.088 and  $0.021 \text{ s}^{-1}$ , respectively), indicating the high intrinsic activity of  $\text{Ni}_2\text{Fe}_1\text{-LDH/rGO/NF}$ . All the above results further justify the excellent electrochemical properties of  $\text{Ni}_2\text{Fe}_1\text{-LDH/rGO/NF}$ .

Given that  $\text{Ni}_2\text{Fe}_1\text{-LDH/rGO/NF}$  can effectively be used for the OER and HER, a two-electrode alkaline electrolytic cell with  $\text{Ni}_2\text{Fe}_1\text{-LDH/rGO/NF}$  as both the anode and cathode was constructed to investigate the overall water splitting performance. As shown in Fig. 6A, the formed two-electrode alkaline electrolytic cell needs only 1.62 and 2.06 V to achieve 10 and  $100 \text{ mA cm}^{-2}$ , respectively. Compared with other reports, the activity of  $\text{Ni}_2\text{Fe}_1\text{-LDH/rGO/NF}$  is better than or at least equal to

that of other non-precious transition metal materials for overall water splitting (Fig. 6D and Table S7, ESI†). Moreover, the chronoamperometry measurements of  $\text{Ni}_2\text{Fe}_1\text{-LDH/rGO/NF}$  at 10 and  $100 \text{ mA cm}^{-2}$  over 24 h showed excellent long-term stability (Fig. 6B). Comparing the LSV curves before and after the test (Fig. 6C), there are only slight overpotential losses of 0.01 and 0.11 V for achieving 10 and  $100 \text{ mA cm}^{-2}$  compared with the initial ones, respectively, further proving the excellent stability toward overall water splitting and the favorable corrosion resistance to the alkaline electrolyte, which are consistent with its superior performance for the OER and HER.

To further demonstrate the excellent catalytic performance of  $\text{Ni}_2\text{Fe}_1\text{-LDH/rGO/NF}$ , we measured the stability of the control sample  $\text{Ni}_2\text{Fe}_1\text{-LDH/NF}$ . It can be seen from Fig. S10 (ESI†) that  $\text{Ni}_2\text{Fe}_1\text{-LDH/NF}$  exhibits excellent stability at low current density, but its stability is significantly reduced at high current density. This can be attributed to the lack of the anchor chain effect provided by rGO, reducing the mechanical stability of the catalyst. In addition, the performance reduction of  $\text{Ni}_2\text{Fe}_1\text{-LDH/NF}$  is larger than that of  $\text{Ni}_2\text{Fe}_1\text{-LDH/rGO/NF}$  after the stability tests. The overpotential for the OER of  $\text{Ni}_2\text{Fe}_1\text{-LDH/NF}$  at 10 and  $100 \text{ mA cm}^{-2}$  decreased by 21 and 63 mV, respectively, and it decreased by 55 and 93 mV for the HER, and decreased by 0.06 and 0.17 V for overall water splitting. These findings can be

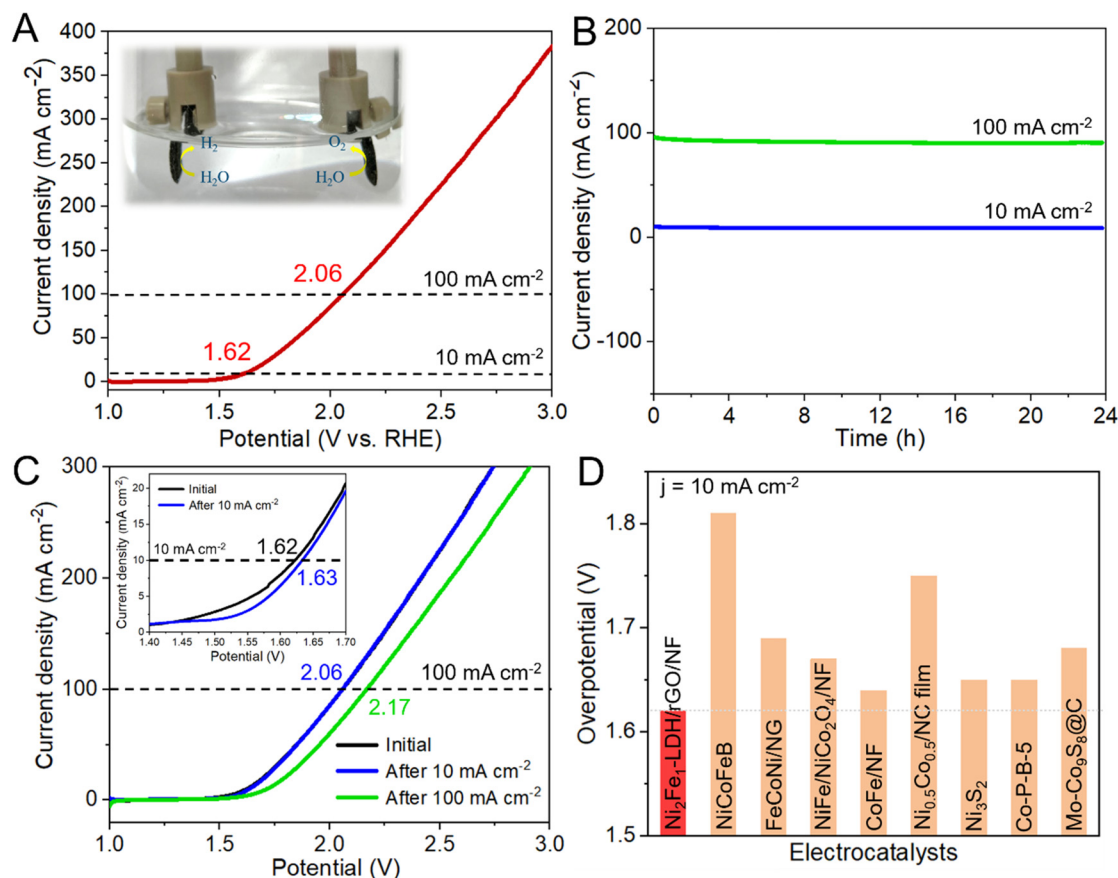
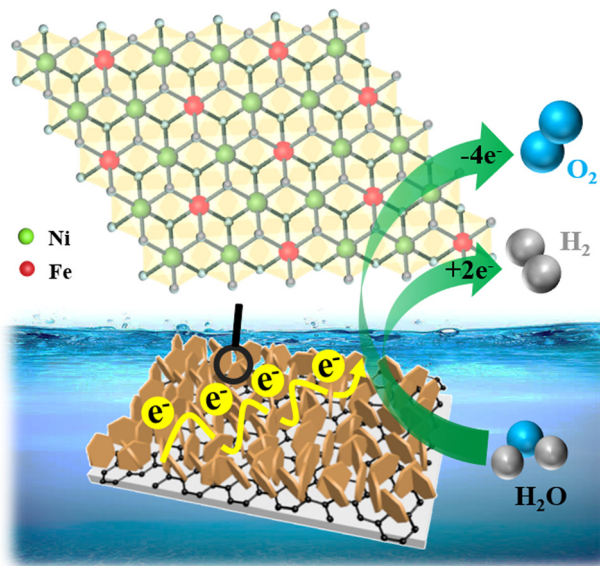


Fig. 6 (A) LSV curve of  $\text{Ni}_2\text{Fe}_1\text{-LDH/rGO/NF}$  in a two-electrode system for overall water splitting. (B) Chronoamperometry measurement (24 h) of  $\text{Ni}_2\text{Fe}_1\text{-LDH/rGO/NF}$ . (C) LSV curves before and after the test. (D) Comparison with other electrocatalysts at  $10 \text{ mA cm}^{-2}$ .





Scheme 2 Diagram of the mechanism of the nanosheet-array-like  $\text{Ni}_2\text{Fe}_1\text{-LDH/rGO/NF}$  electrocatalyst.

attributed to the greatly reduced electrical conductivity and the elevated reaction energy barrier of the catalyst without the contribution of rGO, thus reducing the catalytic performance. In addition, other powder catalysts need to be fixed on the substrate with the help of a binder, so the active sites will be partially covered, and the electrical conductivity and bonding strength will be greatly reduced. Thus, it can be inferred that its stability is far inferior to that of the sample grown directly on NF. Based on the above results, the reasons for the optimal catalytic performance and stability of  $\text{Ni}_2\text{Fe}_1\text{-LDH/rGO/NF}$  can be summarized.

The superior electrocatalytic performance of  $\text{Ni}_2\text{Fe}_1\text{-LDH/rGO/NF}$  may benefit from the following aspects (Scheme 2): (1) the unique nanosheet array morphology with open channels providing a large number of active sites, higher surface area, a highly open pore structure, more electron transport paths and beneficial contact area for the electrolyte and electrode. (2) Strong synergistic interaction between  $\text{Ni}_2\text{Fe}_1\text{-LDH}$  and rGO/NF, with the effective combination of the two parts greatly improving the dispersibility and avoiding the stacking of  $\text{Ni}_2\text{Fe}_1\text{-LDH}$  nanosheets. Additionally, the synergy between the Ni and Fe cores can effectively improve the reaction kinetics and electrical conductivity, which in turn leads to the efficient performance of  $\text{Ni}_2\text{Fe}_1\text{-LDH/rGO/NF}$ . (3) The vertically staggered growth of  $\text{Ni}_2\text{Fe}_1\text{-LDH}$  on the rGO/NF substrate could also improve the stability of the composite and increase the rate of bubble detachment, thus further improving the kinetics of both the OER and HER and the efficiency and stability of the subsequent reactions. All the above advantages make  $\text{Ni}_2\text{Fe}_1\text{-LDH/rGO/NF}$  an excellent catalyst with outstanding electrocatalytic activity and long-term stability.

## Conclusions

We prepared a series of highly efficient bifunctional electrocatalytic composites,  $\text{Ni}_x\text{Fe}_1\text{-LDH/rGO/NF}$  ( $x = 3, 2, 1$ ), with

vertically staggered  $\text{NiFe-LDH}$  nanosheets grown on nickel foam uniformly modified with rGO through a simple hydrothermal method. The as-prepared nanosheet-array-like composites show excellent electrocatalytic performance for the OER and HER. In particular, for the OER, HER and overall water splitting in 1 M KOH,  $\text{Ni}_2\text{Fe}_1\text{-LDH/rGO/NF}$  requires only 228 mV, 109 mV and 1.62 V at  $10 \text{ mA cm}^{-2}$ , respectively.  $\text{Ni}_2\text{Fe}_1\text{-LDH/rGO/NF}$  also has long-term stability over 24 h during the three reactions. Its excellent electrocatalytic performance can be ascribed to: (1) the unique nanosheet-array-like structure with open channels providing numerous active sites; (2) the synergy between  $\text{Ni}_2\text{Fe}_1\text{-LDH}$  and rGO, which improves the electrical conductivity; (3) the vertically staggered growth of  $\text{Ni}_2\text{Fe}_1\text{-LDH}$  on the substrate, which is conducive for bubble release during the test process and thus greatly improves the stability. The strategy has clear advantages in the research of electrolytic water catalysts, and it can also be used to fabricate other transition metal electrocatalysts for application to various catalysis fields, including electrocatalysis.

## Author contributions

Kun Wang: investigation, formal analysis, data curation, writing – original draft, writing – review & editing. Jiawei Guo: investigation, formal analysis, writing – review & editing. Hui Zhang: conceptualization, formal analysis, funding acquisition, project administration, writing – review & editing, resources, supervision.

## Conflicts of interest

There are no conflicts to declare.

## Acknowledgements

The authors greatly appreciate the financial support by the National Natural Science Foundation of China (21878007 and 21838007).

## References

- 1 S. Zhu, G. Duan, C. Chang, Y. Chen, Y. Sun, Y. Tang, P. Wan and J. Pan, *ACS Sustainable Chem. Eng.*, 2020, **8**, 9885–9895.
- 2 F. Dionigi and P. Strasser, *Adv. Energy Mater.*, 2016, **6**, 1600621.
- 3 L. Lv, Z. Yang, K. Chen, C. Wang and Y. Xiong, *Adv. Energy Mater.*, 2019, **9**, 1803358.
- 4 B. Liu, Y. Wang, H. Peng, R. Yang, Z. Jiang, X. Zhou, C. Lee, H. Zhao and W. Zhang, *Adv. Mater.*, 2018, **30**, 1803144.
- 5 N. Suen, S. Hung, Q. Quan, N. Zhang, Y. Xu and H. Chen, *Chem. Soc. Rev.*, 2017, **46**, 337.
- 6 H. Over, *ACS Catal.*, 2021, **11**, 8848–8871.
- 7 O. Mabayoje, A. Shoola, B. Wygant and C. Mullins, *ACS Energy Lett.*, 2016, **1**, 195–201.
- 8 P. Du and R. Eisenberg, *Energy Environ. Sci.*, 2012, **5**, 6012–6021.



- 9 M. W. Louie and A. T. Bell, *J. Am. Chem. Soc.*, 2013, **135**, 12329–12337.
- 10 L. Wu, F. Zhang, S. Song, M. Ning, Q. Zhu, J. Zhou, G. Gao, Z. Chen, Q. Zhou, X. Xing, T. Tong, Y. Yao, J. Bao, L. Yu, S. Chen and Z. Ren, *Adv. Mater.*, 2022, **34**, 2201774.
- 11 L. Yu, H. Zhou, J. Sun, F. Qin, F. Yu, J. Bao, Y. Yu, S. Chen and Z. Ren, *Energy Environ. Sci.*, 2017, **10**, 1820–1827.
- 12 D. Friebel, M. Louie, M. Bajdich, K. Sanwald, Y. Cai, A. Wise, M. Cheng, D. Sokaras, T. Weng, R. AlonsoMori, R. Davis, J. Bargar, J. Nørskov, A. Nilsson and A. Bell, *J. Am. Chem. Soc.*, 2015, **137**, 1305–1313.
- 13 S. Ye, Z. Shi, J. Feng, Y. Tong and G. Li, *Angew. Chem., Int. Ed.*, 2018, **57**, 2672–2676.
- 14 M. McBriarty, G. Rudorff, J. Stubbs, P. Eng, J. Blumberger and K. Rosso, *J. Am. Chem. Soc.*, 2017, **139**, 2581–2584.
- 15 L. Cao, J. Wang, D. Zhong and T. Lu, *J. Mater. Chem. A*, 2018, **6**, 3224–3230.
- 16 Y. Zeng, Y. Wang, G. Huang, C. Chen, L. Huang, R. Chen and S. Wang, *Chem. Commun.*, 2018, **54**, 1465–1468.
- 17 H. Liu, X. Ma, Y. Rao, Y. Liu, J. Liu, L. Wang and M. Wu, *ACS Appl. Mater. Interfaces*, 2018, **10**, 10890–10897.
- 18 V. S. Kale, U. Sim, J. Yang, K. Jin, S. I. Chae, W. J. Chang, A. K. Sinha, H. Ha, C.-C. Hwang, J. An, H.-K. Hong, Z. Lee, K. T. Nam and T. Hyeon, *Small*, 2017, **13**, 1603893.
- 19 J. Yu, G. Cheng and W. Luo, *Nano Res.*, 2018, **11**, 2149–2158.
- 20 B. Zhang, C. Xiao, S. Xie, J. Liang, X. Chen and Y. Tang, *Chem. Mater.*, 2016, **28**, 6934–6941.
- 21 J. Yu, Q. Wang, D. O'Hare and L. Sun, *Chem. Soc. Rev.*, 2017, **46**, 5950–5974.
- 22 L. Yu, J. Xiao, C. Huang, J. Zhou, M. Qiu, Y. Yu, Z. Ren, C.-W. Chu and J. C. Yu, *Proc. Natl. Acad. Sci. U. S. A.*, 2022, **119**, e2202382119.
- 23 J. Zhang, J. Liu, L. Xi, Y. Yu, N. Chen, S. Sun, W. Wang, K. Lange and B. Zhang, *J. Am. Chem. Soc.*, 2018, **140**, 3876–3879.
- 24 P. M. Bodhankar, P. B. Sarawade, G. Singh, A. Vinu and D. S. Dhawale, *J. Mater. Chem. A*, 2021, **9**, 3180–3208.
- 25 P. Liu, S. Yang, B. Zhang and H. Yang, *ACS Appl. Mater. Interfaces*, 2016, **8**, 34474–34481.
- 26 W. Huang, X. Ma, H. Wang, R. Feng, J. Zhou, P. Duchesne, P. Zhang, F. Chen, N. Han, F. Zhao, J. Zhou, W. Cai and Y. Li, *Adv. Mater.*, 2017, **29**, 1703057.
- 27 T. Li, S. Li, Q. Liu, Y. Tian, Y. Zhang, G. Fu and Y. Tang, *ACS Sustainable Chem. Eng.*, 2019, **7**, 17950–17957.
- 28 H. Begum and S. Jeon, *Int. J. Hydrogen Energy*, 2018, **43**, 5522–5529.
- 29 Y. Hou, M. Lohe, J. Zhang, S. Liu, X. Zhuang and X. Feng, *Energy Environ. Sci.*, 2016, **9**, 478–483.
- 30 D. Xia, L. Zhou, S. Qiao, Y. Zhang, D. Tang, J. Liu, H. Huang, Y. Liu and Z. Kang, *Mater. Res. Bull.*, 2016, **74**, 441–446.
- 31 J. Ji, L. Zhang, H. Ji, Y. Li, X. Zhao, X. Bai, X. Fan, F. Zhang and R. Ruoff, *ACS Nano*, 2013, **7**, 6237–6243.
- 32 X. Lu and C. Zhao, *Nat. Commun.*, 2015, **6**, 6616.
- 33 X. Zhu, C. Tang, H. Wang, B. Li, Q. Zhang, C. Li, C. Yang and F. Wei, *J. Mater. Chem. A*, 2016, **4**, 7245–7250.
- 34 Z. Lu, W. Xu, W. Zhu, Q. Yang, X. Lei, J. Liu, Y. Li, X. Sun and X. Duan, *Chem. Commun.*, 2014, **50**, 6479–6482.
- 35 M. Li, R. Jijie, A. Barras, P. Roussel, S. Szunerits and R. Boukherroub, *Electrochim. Acta*, 2019, **302**, 1–9.
- 36 J. Guo, Z. Wei, K. Wang and H. Zhang, *Int. J. Hydrogen Energy*, 2021, **46**, 27529–27542.
- 37 J. Yu, G. Cheng and W. Luo, *J. Mater. Chem. A*, 2017, **5**, 11229–11235.
- 38 Y. Zou, B. Xiao, J. Shi, H. Hao, D. Ma, Y. Lv, G. Sun, J. Li and Y. Cheng, *Electrochim. Acta*, 2020, **348**, 136339.
- 39 J. Xu, S. Gai, F. He, N. Niu, P. Gao, Y. Chen and P. Yang, *J. Mater. Chem. A*, 2014, **2**, 1022–1031.
- 40 L. Dou, T. Fan and H. Zhang, *Catal. Sci. Technol.*, 2015, **5**, 5153–5167.
- 41 M. Li, J. Zhu, L. Zhang, X. Chen, H. Zhang, F. Zhang, S. Xu and D. Evans, *Nanoscale*, 2011, **3**, 4240–4246.
- 42 G. Zhang, Y. Li, Y. Zhou and F. Yang, *ChemElectroChem*, 2016, **3**, 1927–1936.
- 43 L. Zhang, R. Zhang, R. Ge, X. Ren, S. Hao, F. Xie, F. Qu, Z. Liu, G. Du, A. Asiri, B. Zheng and X. Sun, *Chem. – Eur. J.*, 2017, **23**, 11499–11503.
- 44 D. Yang, A. Velamakanni, G. Bozoklu, S. Park, M. Stoller, R. Piner, S. Stankovich, I. Jung, D. Field, C. Ventrice and R. Ruoff, *Carbon*, 2009, **47**, 145–152.
- 45 H. Wang, E. Feng, Y. Liu and C. Zhang, *J. Mater. Chem. A*, 2019, **7**, 7777–7783.
- 46 L. Yu and Z. Ren, *Mater. Today Phys.*, 2020, **14**, 100253.
- 47 J. Zhao, J. Zhang, Z. Li and X. Bu, *Small*, 2020, **16**, 2003916.
- 48 Q. Zhang, Z. Jiang, B. Tackett, S. Denny, B. Tian, X. Chen, B. Wang and J. Chen, *ACS Catal.*, 2019, **9**, 2415–2422.
- 49 W. Liu, X. Hu, H. Li and H. Yu, *Small*, 2018, **14**, 1801878.

